Impact of the neutron matter equation of state on neutron skins and neutron drip lines in chiral effective field theory

Francesca Sammarruca and Yevgen Nosyk

Phys. Rev. C **94**, 044311 — Published 17 October 2016

DOI: 10.1103/PhysRevC.94.044311

Impact of the neutron matter equation of state on neutron skin and neutron drip lines in chiral effective field theory

Francesca Sammarruca and Yevgen Nosyk
Physics Department, University of Idaho, Moscow, ID 83844-0903, U.S.A.
(Dated: September 4, 2016)

We present predictions of the binding energy per nucleon and the neutron skin thickness in highly neutron-rich isotopes of Oxygen, Magnesium, and Aluminum. The calculations are carried out at and below the neutron drip line as predicted by our model. The nuclear properties are obtained *via* an energy functional whose input is the equation of state of isospin-asymmetric infinite matter. The latter is based on a microscopic derivation of the energy per particle in neutron matter applying chiral few-nucleon forces together with a phenomenological model for the equation of state of symmetric nuclear matter. We highlight the impact of the neutron matter equation of state at different orders of chiral effective field theory on neutron skins and the binding energy per particle and quantify the uncertainty carried by our predictions.

I. INTRODUCTION

The behavior of the nuclear force in the medium is a complex problem. While the typical arena to test many-body theories is provided by finite nuclei, the system known as infinite nuclear matter is a suitable environment to gain insight into the nature of nuclear interactions in the medium. Typically, nuclear matter is characterized by the energy per particle in such system, known as the equation of state (EoS). In the presence of different concentrations of neutron and protons, the symmetry energy term appears in the EoS, whose density dependence is well known to play an outstanding role in the structure and dynamics of neutron-rich systems. This paper is part of systematic efforts in our group to explore the EoS through various applications, ranging from neutron skins to neutron stars [1].

Naturally, experimental constraints on the EoS are necessary, and those are extracted from measurements of observables which have been identified as being sensitive to the EoS (see, for instance, Ref. [2]). Among those is the neutron skin thickness, which can be obtained from measurements of the neutron distribution. Thanks to the experimental program at the Jefferson Laboratory, in the near future the weak charge density of some nuclei may be measured accurately. In fact, the first of such observations was completed and yielded a value of $0.33^{+0.16}_{-0.18}$ fm for the neutron skin thickness in ^{208}Pb [3]. We understand that plans are in progress to repeat the experiment aiming at a much smaller uncertainty, and, potentially, perform a similar experiment to extract the skin of ^{48}Ca [3].

The location of the neutron drip lines is another issue of great contemporary interest which is closely related to the nature of the EoS for neutron-rich matter. If a nucleus is extremely neutron-rich, nuclear binding may become insufficient to hold it together and the neutron separation energy, defined as $S_n = B(Z,N) - B(Z,N-1)$, where B is the binding energy, can be negative, indicating that the last neutron has become unbound. (A similar definition applies to the proton drip lines and the proton separation energy, but here we focus on neutron-rich systems.) At this time, the neutron drip line is experimentally accessible only for light nuclei. However, thanks to the recent developments of radioactive beam (RB) facilities, soon it may become possible to explore the stability lines of nuclei ranging from light to very heavy. Note, also, that nuclei beyond the neutron drip lines can exist in the crust of neutron stars. Those nuclei are believed to determine, for instance, the dynamics of superfluid neutron vortices, which, in turn, control the rotational properties of the star. In short, understanding the properties of nuclei with extreme neutron-to-proton ratios is an important and challenging problem for both rare isotope beam experiments and theoretical models.

To provide useful guidance to experiments, predictions should be accompanied by appropriate theoretical uncertainties. With regard to that (and more), chiral effective theory (EFT) [4, 5] has appealing features: it is based on the symmetries of low-energy QCD while using degrees of freedom appropriate for low-energy nuclear physics. Furthermore, and equally important, it allows for a systematic improvement of the predictions and a controlled theoretical error. Therefore, in spite of the (still broad) popularity of meson-theoretic interactions for modern calculations of nuclear structure and reactions, chiral EFT has become established as a more fundamental and model-independent approach. In EFT, long-range physics is determined by the interaction of pions and nucleons together with the (broken) symmetries of QCD, whereas short-range physics is included through "contact terms" and the process of renormalization. Together with an organizational scheme to rank-order the various contributions, known as power counting, two- and few-nucleon forces emerge on an equal footing in a controlled hierarchy.

In this paper, we focus on the question of how the neutron matter (NM) EoS impacts the formation of the neutron skin and the binding energy per particle, which, through the neutron separation energy, determines the location of the drip lines, at different orders of chiral EFT.

We will consider very neutron-rich isotopes of Oxygen, Magnesium, and Aluminum. For the Oxygen isotopic chain,

currently ^{25}O and ^{26}O are at the limit of experimental availability [6], with ^{26}O found to be just unbound [7]. With regard to Magnesium and Aluminum, ^{40}Mg and ^{42}Al are predicted to be drip line nuclei [8, 9], suggesting that the drip lines may be located towards heavier isotopes in this region of the nuclear chart.

The paper is organized as follows: To ensure that the manuscript is self-contained, in Section II we give a brief review of the few-body forces we apply, whereas in Section III we describe our approach to the energy per particle in neutron-rich matter, and how the latter is used in a liquid-drop-based functional in order to obtain nuclear energies and radii. We describe how we estimate the theoretical uncertainties in our calculations, particularly those of EFT origin. Results and discussion are presented in Section IV, while our conclusions are summarized in Section V.

II. DESCRIPTION OF THE FEW-NUCLEON FORCES

Before moving to the description of our calculations in nucleonic matter, in this section we review briefly the few-nucleon forces as we will apply them in Section III. With regard to 3NFs, only those which do not vanish in NM will actually be employed here, although the following remarks may be somewhat broader. For additional details, see Ref. [10].

A. The chiral two-body force

In the present investigation we consider nucleon-nucleon (NN) potentials at order $(Q/\Lambda_\chi)^0$, $(Q/\Lambda_\chi)^2$, $(Q/\Lambda_\chi)^3$ and $(Q/\Lambda_\chi)^4$ in the chiral power counting, where Q denotes the low-energy scale set by a typical external nucleon momenta or the pion mass and Λ_χ is the chiral symmetry breaking scale. Chiral NN potentials at NLO and N^{2}LO (order $(Q/\Lambda_\chi)^2$) and $(Q/\Lambda_\chi)^3$, respectively) have been constructed in Ref. [11] for several values of the cutoff, Λ, in the regulator function

$$f(p',p) = exp[-(p'/\Lambda)^{2n} - (p/\Lambda)^{2n}] \, . \tag{1}$$

When the chiral order and the cutoff scale are changed, the low-energy constants in the two-nucleon sector are refitted to elastic NN scattering phase shifts and the deuteron properties. The low-energy constants $c_{1,3,4}$ associated with the $\pi\pi NN$ contact couplings of the $\mathcal{L}^{(2)}_{\pi N}$ chiral Lagrangian can be extracted from πN or NN scattering data. The potentials we use here [11–13] take the range determined in πN analyses as a starting point. The reader should consult Ref. [13] for details on the fitting procedure.

Although two-body scattering phase shifts can be described well at NLO up to a laboratory energy of about 100 MeV [11] while the N^{2}LO potential fits the NN data up to 200 MeV, high-precision quality is not possible until next-to-next-to-next-to-leading order (N^{3}LO) [12, 13]. The potential at leading order (LO) [13] describes NN data poorly, but we include it in this analysis nevertheless as it may shed additional light on the order-by-order pattern of the predictions.

In what follows, we will employ the chiral NN potentials from Refs. [11–13] with cutoff parameter equal to 450 MeV and n=2 (for LO) or n=3 (for the other orders).

B. The chiral three-nucleon force

The leading three-nucleon force is encountered at third order in the chiral power counting and is expressed as the sum of three contributions, whose corresponding diagrams are shown in Fig. 1, labeled as (a), (b), (c), respectively. These contributions are: the long-range two-pion-exchange part with $\pi\pi NN$ vertex proportional to the low-energy constants c_1, c_3, c_4, the medium-range one-pion exchange diagram proportional to the low-energy constant c_D, and the short-range contact term proportional to c_E.

The inclusion of 3NFs is greatly facilitated by employing the density-dependent NN interaction derived in Refs. [14, 15] from the N^{2}LO chiral three-body force. This effective interaction is obtained by summing one particle-line over the occupied states in the Fermi sea. Ignoring small contributions [16] depending on the center-of-mass momentum, the operator structure of the NN interaction is identical to the one in free space. For symmetric nuclear matter all three-body forces contribute, while for pure neutron matter only terms proportional to the low-energy constants c_1 and c_3 are nonvanishing [15, 16].

While efforts are in progress to improve the status of our calculations, the current "N^{3}LO" study is limited to the inclusion of the N^{2}LO three-body force together with the N^{3}LO two-body force. In Refs. [26, 27], calculations of the neutron matter energy per particle at N^{3}LO show a small effect (of about -0.5 MeV) from the N^{3}LO 3NF at

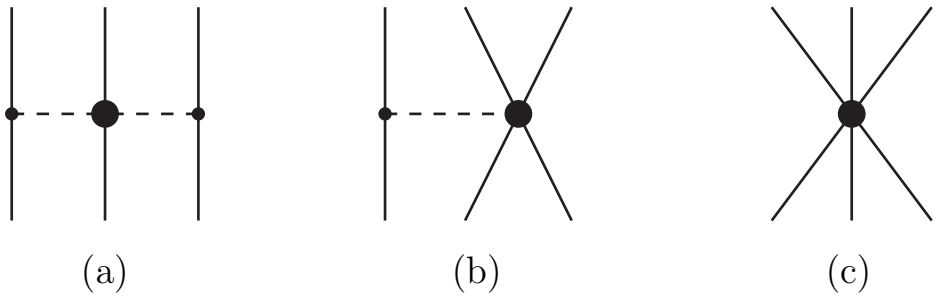

FIG. 1: Diagrams of the 3NF at N^{2}LO. See text for more details.

saturation density for the potentials of our purview [13]. Most recently, the small size of the contribution from the 3NF at N^{3}LO in NM with the potential of Ref. [12] has been confirmed [28]. The inclusion of the 3NF at N^{3}LO in nuclear matter, on the other hand, necessitates a refitting of the c_D and c_E low-energy constants, a non-trivial task still to be completed. With regard to the c_i ($i = 1, 3$), for the potential under our present consideration their values are $c_1 = -0.81$ and $c_3 = -3.40$ at both N2LO and N3LO [13], as determined to best reproduce NN data consistent with πN analyses. The same values are used in the leading 3NF.

It may be useful to make an additional comment concerning the density-dependent effective 3NF from Refs. [14, 15] which we use. The latter is derived employing nonlocal regulators, unlike what is done when constraining the c_D and c_E LECs from genuine 3NFs in the three-nucleon system [19–25], a procedure which has been part of our general scheme [10]. This inconsistency, though, will not impact our present NM results, due to the absence of contributions proportional to c_D and c_E in the pure neutron system.

III. THE MANY-BODY SYSTEM

A. Isospin-asymmetric matter

A variety of many-body methods are available and have been used extensively to calculate the EoS of nucleonic matter. They include: the coupled-cluster method, many-body perturbation, variational Monte Carlo or Green's function Monte Carlo methods.

In computing the EoS, we employ the nonperturbative particle-particle (pp) ladder approximation, namely the leading contribution in the usual hole-line expansion of the energy per particle. To estimate the uncertainty associated with this choice, in Ref. [10] we compared with Refs. [29, 30] and determined that the effect of using a nonperturbative approach beyond pp correlations is negligible in neutron matter (the focal point of this work) and about 1 MeV per nucleon in symmetric matter around saturation density.

B. Application in finite nuclei

In order to link the EoS of asymmetric matter to an actual nucleus, we proceed as described in earlier work [31]. Namely, we write the energy of a sperically symmetric nucleus *via* an energy functional based upon the semi-empirical mass formula: energy of a (spherical) nucleus as

$$E(Z,A) = \int d^3r\ e(\rho,\alpha)\rho(r) + \int d^3r f_0(|\nabla\rho|^2 + \beta|\nabla\rho_I|^2) + \frac{e^2}{4\pi\epsilon_0}(4\pi)^2 \int_0^\infty dr' r' \rho_p(r') \int_0^{r'} dr r^2 \rho_p(r)\ . \tag{2}$$

Note that the integrand in the first term is the isospin-asymmetric equation of state,

$$e(\rho,\alpha) = e(\rho,\alpha=0) + e_{sym}\alpha^2\ , \tag{3}$$

with e_{sym} the symmetry energy. In the above equation, ρ and ρ_I are defined as $\rho_n + \rho_p$ and $(\rho_n - \rho_p)$, respectively, and α represents the neutron excess, $\alpha = \rho_I/\rho$. We take the constant f_0 in Eq. (1) equal to 60 $MeV\ fm^5$, consistent with Ref. [32], and disregard the term with the coefficient β [33] because we found that its contribution was negligible. The impact of varying the parameter f_0 will be addressed later.

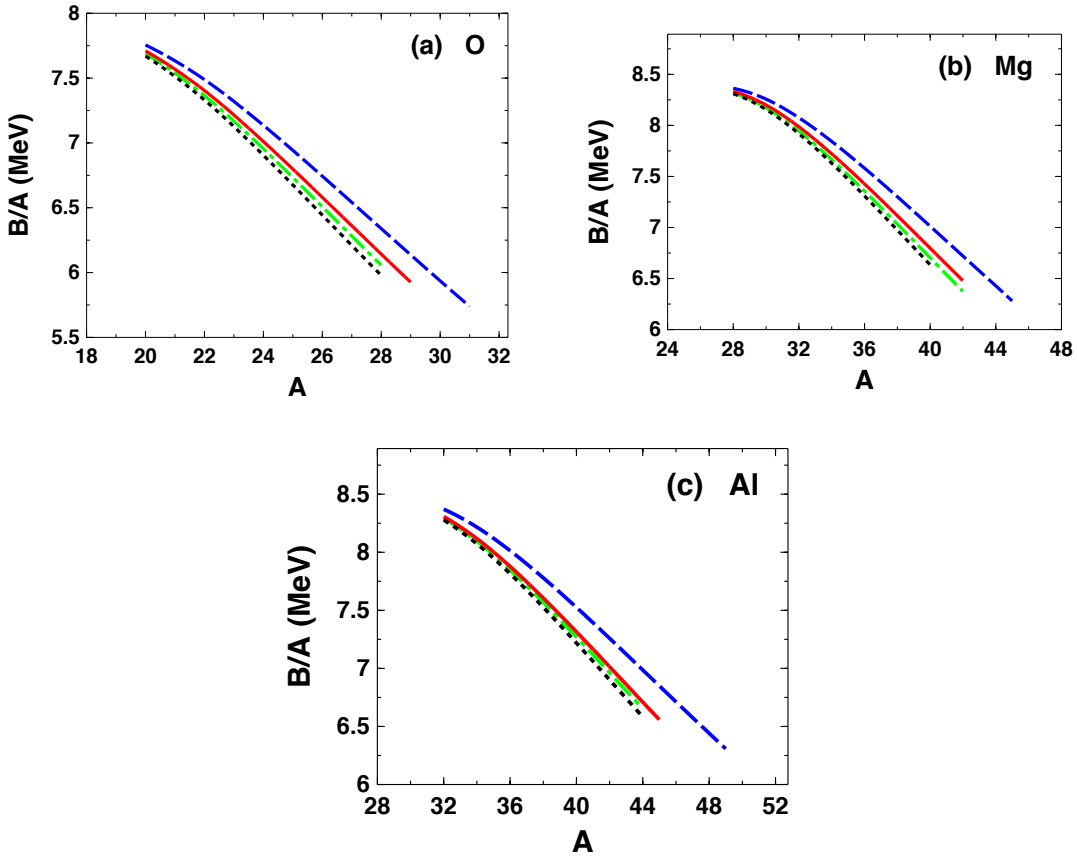

FIG. 2: (Color online) (a): Binding energy per nucleon in neutron-rich isotopes of Oxygen *vs.* the mass number with increasing order of chiral EFT. Dotted black line: LO; Dashed blue: NLO; dash-dotted green: N2LO; Solid red: N3LO. (b): As in (a) for Magnesium; (c): As in (a) for Aluminum. The various orders shown in the figure refer to the microscopic neutron matter equation of state, whereas a phenomenological parametrization is adopted for the equation of state of symmetric matter. See text for details.

The proton and neutron density functions are obtained by minimizing the value of the energy, Eq. (2), with respect to the paramaters of Thomas-Fermi distributions for proton and neutron densities. More specifically, we write

$$\rho_i(r) = \frac{\rho_0}{1 + e^{(r-a_i)/c_i}} \ , \tag{4}$$

with $i = n, p$. The radius and the diffuseness, a_i and c_i, respectively, are optimized by minimization of the energy while ρ_0 is obtained by normalizing the proton(neutron) distribution to $Z(N)$. The skin is defined as

$$S = R_n - R_p \ , \tag{5}$$

where R_n and R_p are the *r.m.s.* radii of the neutron and proton density distributions,

$$R_i = \left(\frac{4\pi}{T} \int_0^\infty \rho_i(r) r^4 \, dr \right)^{1/2} , \tag{6}$$

where T= N or Z. Clearly, this method is not suited to predict detailed quantum structures, such as nuclear shells or pairing effects. On the other hand, our purpose is not to perform detailed structure calculations, but rather to highlight the direct impact of the equation of state on the nuclear properties under consideration.

C. Estimation of the uncertainty

When addressing nucleonic matter or any other many-body system, several sources of theoretical uncertainty need to be considered. The one arising from the choice of the framework for obtaining the EoS was addressed in Sect. III A. Others, inherent to EFT, are:

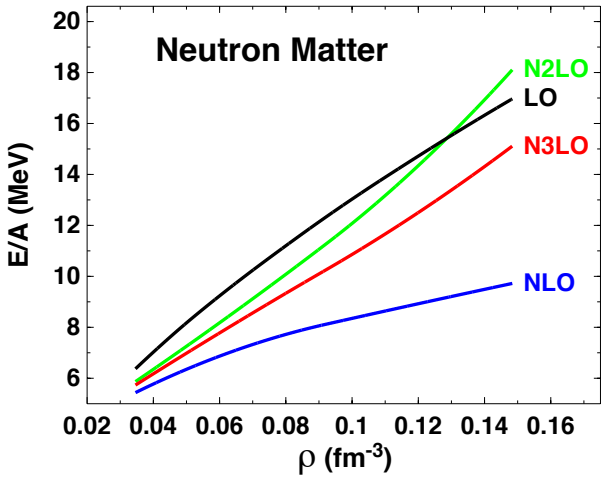

FIG. 3: (Color online) The equation of state of pure neutron matter at various orders of chiral EFT.

- Error in the LECs; This item includes:
  - Short-range (NN) LECs;
  - Long-range (πN) LECs;
- Regulator dependence;
- Truncation error.

We will briefly discuss each of them.

Concerning the NN LECs, we have performed several test Brueckner-Hartree-Fock calculations of nucleonic matter with local high-precision potentials from the Nijmegen group [34] and concluded that the uncertainty arising from error in the experimental determination of NN LECs is much smaller than other errors and can be neglected. With regard to πN LECs, at the two-body level they only impact partial waves where no contacts are available, which, at N^{3}LO, are F waves and higher. Thus, one may expect only minor impact from this uncertainty in the two-nucleon sector. But of course these LECs enter the 3NF, where their uncertainty can have a much larger impact. This point requires a systematic investigation where, for each set of c_i within the allowed experimental error, one constructs NN potentials to be used consistently in the 2NF and the 3NF. It is reassuring to see a recent Roy-Steiner analysis [35] where the authors report very small errors in their determination of πN LECs.

It has been our observation, as well as other authors' [37], that regulator dependence is not a good indicator of the chiral uncertainty at some order, as it tends to underestimate the truncation error. Here, we will determine the latter as explained next. The truncation error is essentially what is left out when terminating the chiral expansion at some order n. If the prediction of observable X at order $n+1$ is available, the truncation error at order n is then

$$\epsilon_n = |X_{n+1} - X_n| \,, \tag{7}$$

which is the $(n+1)$th correction. On the other hand, if X_{n+1} is not available, the truncation error can be estimated to be

$$\epsilon_n = |X_n - X_{n-1}| \frac{Q}{\Lambda} \,, \tag{8}$$

where Q is a momentum typical for the system under consideration or the pion mass, and Λ is the cutoff. Again, we have an expression proportional to $\left(\frac{Q}{\Lambda}\right)^{n+1}$. In our present situation, a reasonable choice for Q is the Fermi momentum corresponding to the average density of a particular nucleus. So, for each nucleus, we calculate the average density from the Thomas-Fermi distributions, Eq. (4), from which we obtain the corresponding Fermi momentum. The above considerations will be used in the next section to quantify the uncertainty of our predictions.

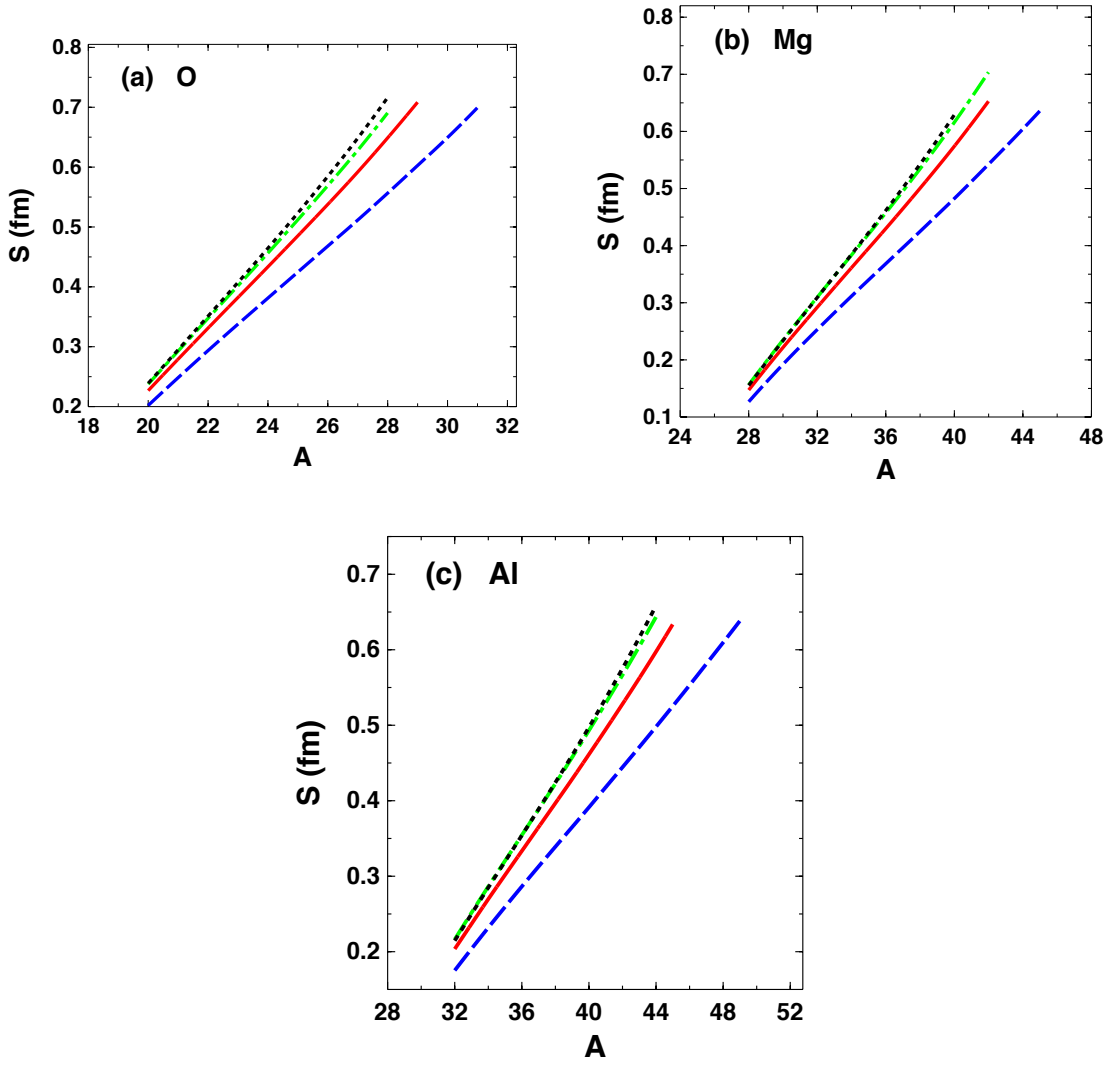

FIG. 4: (Color online) As in Fig. 2, but for the neutron skin thickness S.

IV. RESULTS AND DISCUSSION

In the discussion which follows next, we obtain the neutron matter equation of state microscopically, as described in Ref. [10]. In order to emphasize the role of the pure neutron matter EoS, which is our main goal here, we use an empirical EoS for symmetric nuclear matter (SNM) that we take from Ref. [36]. In this way, we separate out the role of neutron matter pressure and remove any model dependence originating from the details of the saturation point of SNM.

At this time we recall the remarks made at the end of Sect. II B with regard to the contribution from the missing (N^3LO) 3NF expected to be very small in NM at normal density. Nevertheless, even with regard to pure neutron matter, at this stage of our calculations it is not possible to make definite statements about convergence of the EFT predictions from LO to N^3LO, since the EoS for SNM is taken from phenomenology. When the latter, instead, is calculated microscopically, the 3NF should be obtained at N^3LO, consistent with the 2NF, in which case the order-by-order pattern may be different than the one we see here. For these reasons, we limit ourselves to explore the impact of the NM EoS on neutron skins and energies at different orders while avoiding projections about convergence. Note that, for the EoS of NM, the steps from LO to N^2LO are free from inconsistencies.

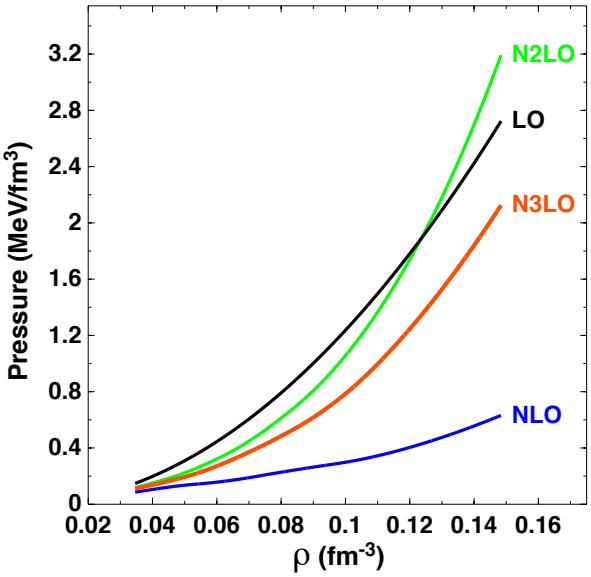

FIG. 5: (Color online) The pressure in pure neutron matter for the interactions considered in Fig. 3.

The phenomenological EoS of SNM is obtained from a Skyrme-type energy density functional and has a realistic saturation point at ρ_0=0.16 fm^{-3} with energy per particle equal to -16.0 MeV [36].

Figure 2 shows the binding energy per nucleon as a function of the mass number for neutron-rich isotopes of Oxygen, Magnesium, and Aluminum. The four curves are obtained at order 0 (LO, dotted black), order 2 (NLO, dashed blue), order 3 (N^{2}LO, dash-dotted green), and order 4 (N^{3}LO, solid red) of chiral EFT in the calculation of the neutron matter EoS. In each case, the curves end where the neutron separation energy, $S_n = B(Z,N) - B(Z,N-1)$, turns negative. We make the following main observations:

- The pattern shown in the figure is consistent with the change in the degree of attraction/repulsion seen in the NM EoS at the corresponding orders and at the low to moderate densities probed by the observables in this study, see Fig. 3. Namely, the most attractive interactions bind the last neutron up to larger values of A.

- The order-by-order pattern is such that differences between consecutive orders become smaller when going from LO to N^{3}LO.

In Fig. 4, the neutron skin thickness is shown as a function of A for the same isotopes and physical interactions as considered in Fig. 2. The largest values of the skin are obtained with the most repulsive NM EoS. Note also how the pressure in neutron matter at the various orders shown in Fig. 5 reveals large differences among the various interactions. The order-by-order pattern is consistent with what we observed for the binding energy. At the low densities (likely to be probed by the skin), the LO and the N^{2}LO interactions yield very similar values for the pressure and the skin.

We provide additional information in Table I, where we made some selections in order to avoid an excessively cumbersome tabulation. For each of the three elements under consideration, we show the smallest value of A from Figs. 2,4 and the value of A (also from Figs. 2,4) for which the separation energy first becomes negative, namely, the first value of A at which one of the three curves is interrupted. (This way, the energies and skins in the tables are comparable with one another order by order, whereas the "drip" A would be different at each order.) The emerging pattern is clear and suggests that the truncation error decreases at the higher orders of the expansion, for both the energy and the skin. Also, at fixed order, the uncertainty is larger for the more neutron-rich systems, most likely reflecting increasing role of the microscopic NM EoS with its corresponding uncertainty.

Concerning the latter, we provide some quantitative information in Table II. As described at the end of Sec. III C, in developing Table I we needed to find an average density relevant for the nuclei included in this investigation. The latter was found to range from about 0.081 to 0.095 fm^{-3}, or, in terms of the Fermi momentum of SNM, from about

Nucleus	Order	B/A with truncation error (MeV)	S with truncation error (fm)
^{20}O	LO	7.670 ± 0.085	0.239 ± 0.037
	NLO	7.755 ± 0.067	0.202 ± 0.036
	N2LO	7.688 ± 0.021	0.238 ± 0.011
	N3LO	7.709 ± 0.01	0.227 ± 0.005
^{28}O	LO	5.978 ± 0.361	0.716 ± 0.159
	NLO	6.339 ± 0.282	0.557 ± 0.134
	N2LO	6.057 ± 0.085	0.691 ± 0.042
	N3LO	6.142 ± 0.040	0.649 ± 0.019
^{28}Mg	LO	8.310 ± 0.053	0.155 ± 0.028
	NLO	8.363 ± 0.044	0.127 ± 0.029
	N2LO	8.319 ± 0.014	0.156 ± 0.009
	N3LO	8.333 ± 0.007	0.147 ± 0.005
^{40}Mg	LO	6.634 ± 0.378	0.621 ± 0.138
	NLO	7.012 ± 0.309	0.483 ± 0.133
	N2LO	6.703 ± 0.094	0.616 ± 0.042
	N3LO	6.797 ± 0.045	0.574 ± 0.020
^{32}Al	LO	8.278 ± 0.093	0.215 ± 0.040
	NLO	8.371 ± 0.078	0.175 ± 0.041
	N2LO	8.293 ± 0.014	0.216 ± 0.013
	N3LO	8.307 ± 0.007	0.204 ± 0.007
^{44}Al	LO	6.582 ± 0.404	0.659 ± 0.161
	NLO	6.986 ± 0.333	0.498 ± 0.146
	N2LO	6.653 ± 0.082	0.644 ± 0.046
	N3LO	6.709 ± 0.027	0.598 ± 0.022

TABLE I: Binding energy per nucleon (B/A) and neutron skin (S), along with their truncation error at each order, for some of the neutron-rich nuclei from Figs. 2,4. See text for more details.

k_F^n (fm^{-1})	Order	E/A with truncation error (MeV)
1.39	LO	12.126 ± 4.10
	NLO	8.027 ± 2.99
	N2LO	11.017 ± 0.95
	N3LO	10.063 ± 0.58

TABLE II: The energy per neutron in NM (E/A) with its truncation error at the indicated chiral orders. The value of the *neutron* Fermi momentum, k_F^n, corresponds approximately to the average density determined earlier for the nuclei under consideration.

1.06 to 1.12 fm^{-1}. Thus, k_F =1.1 fm^{-1} is representative, which translates into the *neutron* Fermi momentum entered in Table II. The Table shows the energy per neutron at the various orders with their truncation error, which has been calculated as explained earlier, with k_F^n as the typical momentum used in Eq. (8).

Finally we like to discuss an uncertainty that is not EFT-related. This is due to variations of the f_0 parameter [32] in the surface term of the liquid droplet functional, Eq. (2), when fitted to β-stable nuclei. This uncertainty is displayed in Table III. The values shown are an average of the predictions obtained with f_0= 60 MeV fm^5 and those with f_0= 70 MeV fm^5 [32] with the error arising from such variation. We see that the uncertainty associated with this parameter is approximately independent of the chiral order. For the energy, it is generally larger than the truncation error, although the latter may dominate at LO. For the skin, on the other hand, it is smaller than or comparable with the truncation error, particularly at the highest order. Note that the error displayed in Table III is not related to the Hamiltonian, whose pattern by chiral order remains the same regardless the value of f_0. The final results including their compounded error (calculated in quadrature) are shown in Table IV.

It is also interesting to mention recent *ab initio* calculations of medium-mass neutron-rich nuclei, ^{48}Ca in particular [38]. There, the neutron skin thickness in ^{48}Ca was predicted with various low-momentum chiral Hamiltonians [39] and found to be nearly independent of the interaction, due to a strong correlation between the point neutron and

Nucleus	Order	B/A (MeV)	S (fm)
^{20}O	LO	7.445 ± 0.226	0.248 ± 0.009
	NLO	7.526 ± 0.230	0.211 ± 0.009
	N2LO	7.463 ± 0.225	0.246 ± 0.008
	N3LO	7.483 ± 0.227	0.236 ± 0.009
^{28}O	LO	5.825 ± 0.153	0.740 ± 0.024
	NLO	6.170 ± 0.170	0.581 ± 0.024
	N2LO	5.904 ± 0.153	0.712 ± 0.021
	N3LO	5.985 ± 0.158	0.671 ± 0.022
^{28}Mg	LO	8.094 ± 0.216	0.162 ± 0.006
	NLO	8.145 ± 0.218	0.133 ± 0.006
	N2LO	8.110 ± 0.210	0.162 ± 0.006
	N3LO	8.117 ± 0.216	0.153 ± 0.006
^{40}Mg	LO	6.489 ± 0.146	0.652 ± 0.022
	NLO	6.851 ± 0.161	0.504 ± 0.022
	N2LO	6.558 ± 0.145	0.636 ± 0.020
	N3LO	6.647 ± 0.150	0.595 ± 0.021
^{32}Al	LO	8.075 ± 0.203	0.223± 0.009
	NLO	8.164 ± 0.207	0.183 ± 0.008
	N2LO	8.091 ± 0.203	0.224 ± 0.008
	N3LO	8.108 ± 0.199	0.212 ± 0.008
^{44}Al	LO	6.443 ± 0.139	0.682 ± 0.023
	NLO	6.831 ± 0.155	0.521 ± 0.023
	N2LO	6.515 ± 0.138	0.665 ± 0.021
	N3LO	6.589 ± 0.121	0.620 ± 0.022

TABLE III: Binding energy per nucleon (B/A) and neutron skin (S) for the same nuclei considered in Table I. The values shown are an average of the predictions obtained with f_0= 60 MeV fm^5 and those obtained with f_0= 70 MeV fm^5 [32] with the error arising from such variation.

proton radii. Here, we have considered a group of interactions at different chiral orders while keeping the properties of SNM fixed. Under the present circumstances, we find that larger NM pressure corresponds to larger neutron skin.

Before closing, we wish to extend the discussion and explore correlations among the main quantities addressed in this investigation. Linear correlations between two variables are usually studied using the Pearson coefficient:

$$\rho(x,y) = \frac{cov(x,y)}{\sigma_x \sigma_y} \ , \tag{9}$$

where the covariance $cov(x,y)$ is defined as

$$cov(x,y) = \sum_{i=1}^{n} \frac{(x_i - \bar{x})(y_i - \bar{y})}{n-1} \ , \tag{10}$$

and $\bar{x}$ and $\bar{y}$ are the average values of the $\{x_i\}$ and $\{y_i\}$ data sets, respectively. σ_x and σ_y are the usual standard deviations. Note that our samples contain only four data, namely the skins at LO to N^{3}LO and the pressure or energy at the corresponding orders (at some chosen, fixed density). This may render the Pearson coefficient, or the identification of a specific fitting function, unreliable. We will show correlations graphically, see Fig. 6. There, we see a positive correlation between skin and either the pressure or the energy per particle in NM. The figure shows the skin of ^{40}Mg, but the behavior is representative for the other nuclei.

To make a similar analysis of how the drip lines correlate with neutron matter pressure or energy, we consider the neutron separation energy, $S_n = B(Z,N) - B(Z,N-1)$, which is chiefly responsible for the location of the driplines. For a particular nucleus, again ^{40}Mg, we calculate $S_n = B(Z=12,N=28) - B(Z=12,N=27)$. The correlation between the separation energy at the four orders and the corresponding pressure and energy in NM are shown in in Fig. 7 on the left side and the right side, respectively. We see a definite anticorrelation of the neutron removal

Nucleus	Order	B/A (MeV)	S (fm)
^{20}O	LO	7.445 ± 0.241	0.248 ± 0.038
	NLO	7.526 ± 0.240	0.211 ± 0.037
	N2LO	7.463 ± 0.226	0.246 ± 0.014
	N3LO	7.483 ± 0.227	0.236 ± 0.010
^{28}O	LO	5.825 ± 0.392	0.740 ± 0.161
	NLO	6.170 ± 0.329	0.581 ± 0.136
	N2LO	5.904 ± 0.175	0.712 ± 0.047
	N3LO	5.985 ± 0.163	0.671 ± 0.029
^{28}Mg	LO	8.094 ± 0.222	0.162 ± 0.029
	NLO	8.145 ± 0.222	0.133 ± 0.031
	N2LO	8.110 ± 0.210	0.162 ± 0.011
	N3LO	8.117 ± 0.216	0.153 ± 0.008
^{40}Mg	LO	6.489 ± 0.405	0.652 ± 0.140
	NLO	6.851 ± 0.348	0.504 ± 0.135
	N2LO	6.558 ± 0.173	0.636 ± 0.047
	N3LO	6.647 ± 0.157	0.595 ± 0.029
^{32}Al	LO	8.075 ± 0.223	0.223 ± 0.041
	NLO	8.164 ± 0.221	0.183 ± 0.042
	N2LO	8.091 ± 0.203	0.224 ± 0.015
	N3LO	8.108 ± 0.199	0.212 ± 0.011
^{44}Al	LO	6.443 ± 0.427	0.682 ± 0.163
	NLO	6.831 ± 0.367	0.521 ± 0.148
	N2LO	6.515 ± 0.161	0.665 ± 0.051
	N3LO	6.589 ± 0.124	0.620 ± 0.031

TABLE IV: Binding energy per nucleon (B/A) and neutron skin (S) for the same nuclei as in Table I with their compounded error.

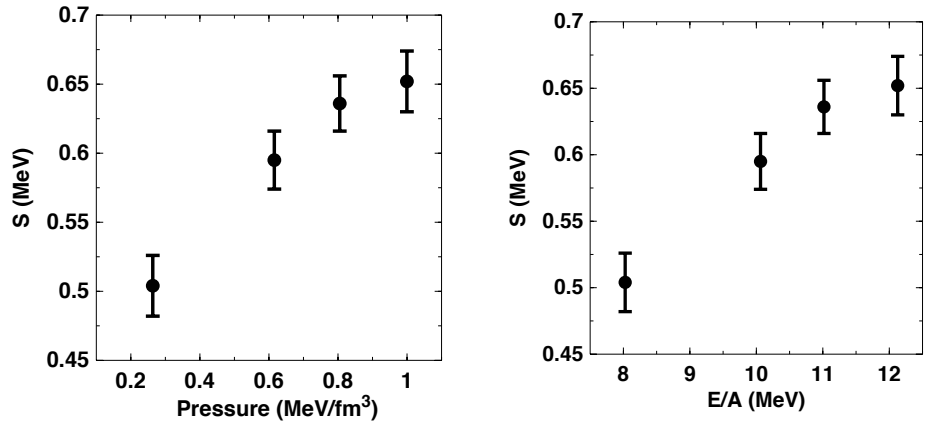

FIG. 6: (Color online) Correlation between the skin, S, and the pressure (left) or the energy in neutron matter (right). The density is fixed and equal to the average density in ^{40}Mg. Skin values as in Table III.

energy with either pressure or energy in NM. Since a smaller separation energy signifies that the drip line is closer, we conclude that either larger NM pressure or larger energy will facilitate the onset of the drip lines.

We like to end with a comparison with currently available empirical information. As mentioned in the Introduction, experimental information on very neutron-rich nuclei, particularly neutron densities, is still scarse, a state of affairs

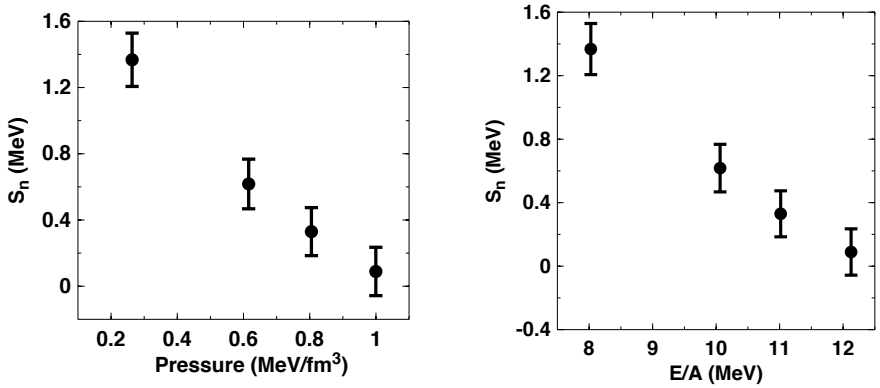

FIG. 7: (Color online) Correlation between the neutron separation energy, S_n, and the pressure (left) or the energy in neutron matter (right). Details are given in the text.

which is expected to improve with measurements at RB facilities and the electroweak program at Jlab. To gain a better insight on how the predictions from our functional compare with available tabulations, experimental or estimated, we consulted the large compilation of nuclear data from Ref. [40]. The values we found for the binding energy per nucleon compare favorably with those in Table IV. For instance, Ref. [40] reports for ^{28}Mg a value of 8.2724 MeV (our predictions at N^{3}LO: 8.117 $\pm$ 0.216 MeV); for ^{40}Mg a value of 6.621 MeV (our predictions at N^{3}LO: 6.647 $\pm$ 0.157 MeV); for ^{20}O a value of 7.568 MeV (our predictions at N^{3}LO: 7.483 $\pm$ 0.227 MeV); for ^{32}Al a value of 8.100 MeV (our predictions at N^{3}LO: 8.108 $\pm$ 0.199 MeV).

As another test of the general validity of the functional method (regardless the EoS), we calculated the binding energy per nucleon and the charge radius for one of the much studied closed-shell nuclei, namely ^{40}Ca. Since this nucleus is isospin-symmetric, the model-dependence of the NM EoS plays only a minor role, if any. We obtain 8.333 $\pm$ 0.200 MeV and 3.504 $\pm$ 0.077 fm for B/A and the charge radius, respectively, to be compared with the empirical values of 8.55 MeV and 3.48 fm. The ab initio prediction for the charge radius of ^{40}Ca is given in Ref. [38] as 3.49(3) fm.

In conclusion, we find that our method is able to produce realistic values for bulk nuclear properties.

V. CONCLUSIONS AND OUTLOOK

The equation of state of infinite matter and its density dependence contain rich information about nucleonic interactions in the medium, which can be extracted through the analysis of EoS-sensitive observables. In this paper, we calculated binding energies and neutron skins for neutron-rich isotopes of three selected elements with a method where the EoS of isospin-asymmetric matter is the crucial input. Our neutron matter EoS are based on chiral nuclear forces constrained by πN and NN data. In order to highlight the role of the pure neutron matter EoS, the calculations employed microscopic equations of state for neutron matter obtained at different orders of chiral EFT, whereas a phenomenological model was adopted for the EoS of symmetric nuclear matter.

We discussed various sources of uncertainty, paying particular attention to truncation errors. Predictions for both the binding energy and the neutron skin show a large truncation error at LO and a much smaller one at N^{3}LO. Thinking specifically of the Hamiltonian, this behavior is encouraging, but complete calculations including consistent 2NF and 3NF, as well as calculations at N^{4}LO, will be crucial to assess a successful path to convergence. We also observed that the uncertainty on the energy related to a free parameter in the functional is typically larger than the smallest truncation error. This is not the case for the neutron skin, where the compounded error remains dominated by the order-by-order pattern. We note, further, that the uncertainty associated with this parameter is uncorrelated with the chiral order, and so it does not hinder our ability to observe a pattern by order, and, hopefully in the near future, a convergence pattern with respect to the Hamiltonian.

We close by reiterating the main motivation for studies such as this one. Our empirical knowledge of nuclear structure at the limits of stability is very limited, a status of affairs which is likely to improve in the near future thanks to the development of radioactive beam facilities. Along with this on-going experimental efforts, it is important

to carry out calculations based on microscopic state-of-the-art nuclear forces. The effective field theory approach is unique in that it allows to estimate the uncertainty of the predictions.

Acknowledgments

This work was supported by the U.S. Department of Energy, Office of Science, Office of Basic Energy Sciences, under Award Number DE-FG02-03ER41270.

[1] F. Sammarruca, *Int. J. Mod. Phys. E* **22**, 1330031 (2013).
[2] M.B. Tsang *et al.*, *Phys. Rev. C* **86**, 015803 (2012); and references therein.
[3] S. Abrahamyan *et al.* (PREX Collaboration), *Phys. Rev. Lett.* **108**, 112502 (2012).
[4] S. Weinberg, *Physics* **96A**, 327 (1979).
[5] S. Weinberg, *Phys. Lett. B* **251**, 288 (1990).
[6] C. Caesar *et al.*, *Phys. Rev. C* **88**, 034313 (2013).
[7] Y. Kondo *et al.*, *Phys. Rev. Lett.* **116**, 102503 (2016).
[8] T. Baumann *et al.*, *Nature* **449**, 1022 (2007).
[9] Paul-Henri Heenen, *Nature* **449**, 992 (2007).
[10] F. Sammarruca, L. Coraggio, J. Holt, N. Itaco, R. Machleidt, and L.E. Marcucci, *Phys. Rev. C* **91**, 054311 (2015).
[11] E. Marji, A. Canul, Q. MacPherson, R. Winzer, Ch. Zeoli, D.R. Entem, and R. Machleidt, *Phys. Rev. C* **88**, 054002 (2013).
[12] D.R. Entem and R. Machleidt, *Phys. Rev. C* **68**, 041001 (2003).
[13] R. Machleidt and D.R. Entem, *Phys. Rep.* **503**, 1 (2011).
[14] J. W. Holt, N. Kaiser, and W. Weise, *Phys. Rev. C* **79**, 054331 (2009).
[15] J. W. Holt, N. Kaiser, and W. Weise, *Phys. Rev. C* **81**, 024002 (2010).
[16] K. Hebeler and A. Schwenk, *Phys. Rev. C* **82**, 014314 (2010).
[17] L. Coraggio, J.W. Holt, N. Itaco, R. Machleidt, L. E. Marcucci, and F. Sammarruca, *Phys. Rev. C* **89**, 044321 (2014).
[18] N. Kaiser, *Eur. Phys. J. A* **48**, 58 (2012).
[19] A. Gardestig and D.R. Phillips, *Phys. Rev. Lett.* **96**, 232301 (2006).
[20] D. Gazit, S. Quaglioni, and P. Navratil, *Phys. Rev. Lett.* **103**, 102502 (2009).
[21] L.E. Marcucci, A. Kievsky, S. Rosati, R. Schiavilla, and M. Viviani, *Phys. Rev. Lett.* **108**, 052502 (2012).
[22] M. Viviani, L. Girlanda, A. Kievsky, and L.E. Marcucci, *Phys. Rev. Lett.* **111**, 172302 (2013).
[23] M. Piarulli, L. Girlanda, L.E. Marcucci, S. Pastore, R. Schiavilla, and M. Viviani, *Phys. Rev. C* **87**, 014006 (2013).
[24] L.E. Marcucci, R. Schiavilla, and M. Viviani, *Phys. Rev. Lett.* **110**, 192503 (2013).
[25] M. Viviani, A. Baroni, L. Girlanda, A. Kievsky, L.E. Marcucci, and R. Schiavilla, *Phys. Rev. C* **89**, 064004 (2014).
[26] T. Krüger, I. Tews, K. Hebeler, and A. Schwenk, *Phys. Rev. C* **88**, 025802 (2013).
[27] I. Tews, T. Krüger, K. Hebeler, and A. Schwenk, *Phys. Rev. Lett.* **110**, 032504 (2013).
[28] C. Drischler, A. Carbone, K. Hebeler, and A. Schwenk, arXiv:1608.05615 [nucl-th].
[29] G. Baardsen *et al.*, *Phys. Rev. C* **88**, 054312 (2013).
[30] G. Hagen *et al.*, *Phys. Rev. C* **89**, 014319 (2014).
[31] F. Sammarruca, *Symmetry* **7**, 1646 (2015); and references therein.
[32] K. Oyamatsu, Kei Iida, and Hiroyuki Koura, arXiv:1005.3183 [nucl-th].
[33] R.J. Furnstahl, *Nucl. Phys. A* **706**, 85 (2002).
[34] V. Stoks, R. Klomp, C. Terheggen, and J. de Swart, Phys. Rev. C **49**, 2950 (1994).
[35] Martin Hoferichter *et al.*, *Phys. Rev. Lett.* **115**, 192301 (2015).
[36] N. Alam, B.K. Agrawal, J.N. De, S.K. Samaddar, G. Coló, *Phys. Rev. C* **90**, 054317 (2014).
[37] E. Epelbaum, H. Krebs, and U.-G. Meissner, *Eur. Phys. J. A* (2015) **51**:53.
[38] G. Hagen *et al.*, *Nature Physics* **12**, 186 (2016).
[39] K. Hebeler, S.K. Bogner, R.J. Furnstahl, A. Nogga, A. Schwenk, *Phys. Rev. C* **83**, 031301 (2011).
[40] G. Audi, M. Wang, A.H. Wapstra, F.G. Kondev, M. MacCormick, X. Xu, and B. Pfeiffer, *Chinese Physics* **C36**, 1287 (2012); G. Audi, M. Wang, A.H. Wapstra, F.G. Kondev, M. MacCormick, X. Xu, and B. Pfeiffer, *Chinese Physics* **C36**, 1603 (2012).